minerals

Article

Spatial Analysis of Structure and Metal Mineralization Based on Fractal Theory and Fry Analysis: A Case Study in Nenjiang−Heihe Metallogenic Belt

Zhonghai Zhao [1,*], Jun Chen [1], Binbin Cheng [1], Yiwen Liu [1], Kai Qiao [1], Xiaomeng Cui [1], Yechang Yin [1] and Chenglu Li [2]

[1] College of Mining, Liaoning Technical University, Fuxin 123000, China
[2] Heilongjiang Institute of Natural Resources Survey, Harbin 150036, China
* Correspondence: zhaozhonghai@lntu.edu.cn

Abstract: Regional tectonics can provide excellent transport channels and precipitation sites for mineralized hydrothermal fluid. Studying the spatial relationship and distribution trends of regional tectonics and metal mineralization has theoretical and practical significance for revealing regional mineralization regularities and guiding mineral exploration. This study considers the Nenjiang-Heihe metallogenic belt, through the fractal box dimension method and Fry analysis, to explore the spatial distribution characteristics and patterns of tectonics. The results were as follows. (1) NE and NW directions are the main tectonic directions in the study area, with high-density areas concentrated in the central-eastern and central-western regions, demonstrating an overall ring-like distribution pattern. (2) Fractal dimensions of the linear structures of the NE and NW directions and the entire study area are 1.543, 1.493, and 1.622, respectively, with a strong coupling relationship between the lineament fractal high-value area and rhombic-grid spatial distribution of known deposits. (3) Gold mineralization shows the NEE and NWW directions as two main mineralization trends; the intersection area is the gold-potential area. The main trend direction of the Cu-Mo metallogenic trend belt is the NNW direction; the intersection area with the NEE direction gold metallogenic trend belt is the Au-Cu-Mo potential mineralization area.

Keywords: tectonic extraction; fractal dimension; lineaments; Fry analysis; Nenjiang–Heihe metallogenic belt

check for updates

Citation: Zhao, Z.; Chen, J.; Cheng, B.; Liu, Y.; Qiao, K.; Cui, X.; Yin, Y.; Li, C. Spatial Analysis of Structure and Metal Mineralization Based on Fractal Theory and Fry Analysis: A Case Study in Nenjiang−Heihe Metallogenic Belt. *Minerals* **2023**, *13*, 313. https://doi.org/10.3390/min13030313

Academic Editor: António Manuel Nunes Mateus

Received: 21 December 2022
Revised: 18 February 2023
Accepted: 19 February 2023
Published: 23 February 2023

1. Introduction

Fracture structure is a critical mineral control factor for hydrothermal deposits. It is the dynamic driving and migration channel of mineralizing fluids, providing the occurrence space for orebody deposition. The spatial coupling of regional fractures and metal mineralization has been a popular research topic, engendering numerous studies [1–8]. To describe the spatial relationship between metal mineralization and regional tectonics, mathematical methods have been proposed, such as the weight-of-evidence method, factor analysis, distance distribution analysis, support vector machines, random forest, fractal theory, and Fry analysis [9–14]. Among them, fractal theory and Fry analysis have been rapidly developed in recent years as effective means to quantitatively analyze fracture structure and reveal the spatial relationship between the distribution of deposits (points) and fractures [10,15,16]. As a quantitative method to describe natural phenomena or objects with irregular shapes or distributions, fractal theory can extract deterministic and regular covariates from complex and disordered patterns to retrieve the mechanism of fractal structure formation and infer the system evolution from stochastic evolutionary processes. The fractal dimension is the dimensional value of a fractal, which is an essential parameter for the quantitative characterization of fractals. The study of fracture structure can quantitatively describe the complexity of the structure, which provides a basis for evaluating mineralization potential.

Therefore, a fracture structure area with a high fractal dimension value is usually closely related to metal mineralization [17–19]. Lei et al. [20] analyzed the fracture structures in the Jiuyi Mountain area in south Hunan Province using the fractal theory box dimension method, and showed that high and low fractal dimension values are consistent with the intensity of mineralization in the area. Ni et al. [18] used fractal and multifractal theory to analyze the spatial distribution and characteristics of lineaments in northeastern Yunnan. Ahmadfaraj et al. [21] predicted the location of copper mineralization sites using the fractal dimensional values of structures in the Savi region of central Iran, determining that the known deposits are located in areas with high fractal dimensional values. Jiang et al. [22] studied the fractal system of fracture structures using the fractal theory box dimension method and showed that the fractal dimension value is indicative of the mineralization potential in the study area.

Fry analysis (i.e., allocentric distance analysis) is an analytical method used to study the spatial distribution of random points and manually evaluate the autocorrelation of the rock strain spatial distribution. It has the advantage of simple and rapid analysis and is widely used to measure the spatial distribution of mineral deposits and infer potential mineral control structures [2,11,15,22–27]. Previous investigators have used Fry analysis to study the spatial distribution of various metal deposits [2,15,24,26,28] and even found that Fry analysis can identify the preferred distribution direction of mineralization in 3D space, which is difficult to identify from the original map [27,29]. At different scales, the spatial relationship and distribution between lineaments and ore deposits (points) can be determined, and the effects of tectonics on mineralization can be explained [2,15].

Fry analysis and fractal theory can be combined for mineral distribution analysis [2], deposit distribution patterns, and mineralization prediction. For example, Carranza et al. [11] and Bie et al. [30] used fractal analysis and Fry analysis to study the spatial patterns of known deposits (points) and the spatial association of various geological features, and traced the prospective mineralized area. Few studies have applied Fry analysis to the distribution pattern of deposits (points) in combination with tectonic fractal methods for the spatial analysis of tectonics and metal mineralization.

The study area is the Duobaoshan-Daxintun national integrated exploration area, as the pilot of the deep exploration. In recent years, with the deepening of prospecting and exploration, large and medium-sized deposits such as Duobaoshan, Tongshan, Sankuanggou, Zhengguang, Sandaowanzi, Yongxin deposits, and many other mineralization points have been discovered. However, in past research most have been limited to the study of typical deposits, geological background, and geological exploration; therefore, it is urgent to carry out metallogenic regularity and prediction research. At the same time, the Nenjiang-Heihe metallogenic belt indicates a complex structure and an excellent regional geological and metallogenic background, which is conducive to the analysis of the fractal dimension and quantitative coupling relationship between the structures and spatial distribution of the deposits. Therefore, we chose the Nenjiang-Heihe metallogenic belt as the research object in this study.

2. Geological Background

Northeast China is located between the North China Craton and the Siberian Craton, in the easternmost part of the Central Asian Orogenic Belt (Figure 1A) [31–34] and consists mainly of a series of microcontinents and continental margin accretionary complex belts of different properties, including the Erguna Block, Xing'an Block, and Songnen–Xilinhot Block, as well as the Jiamusi Block and Xingkai Block from west to east (Figure 1B) [32,35–37].

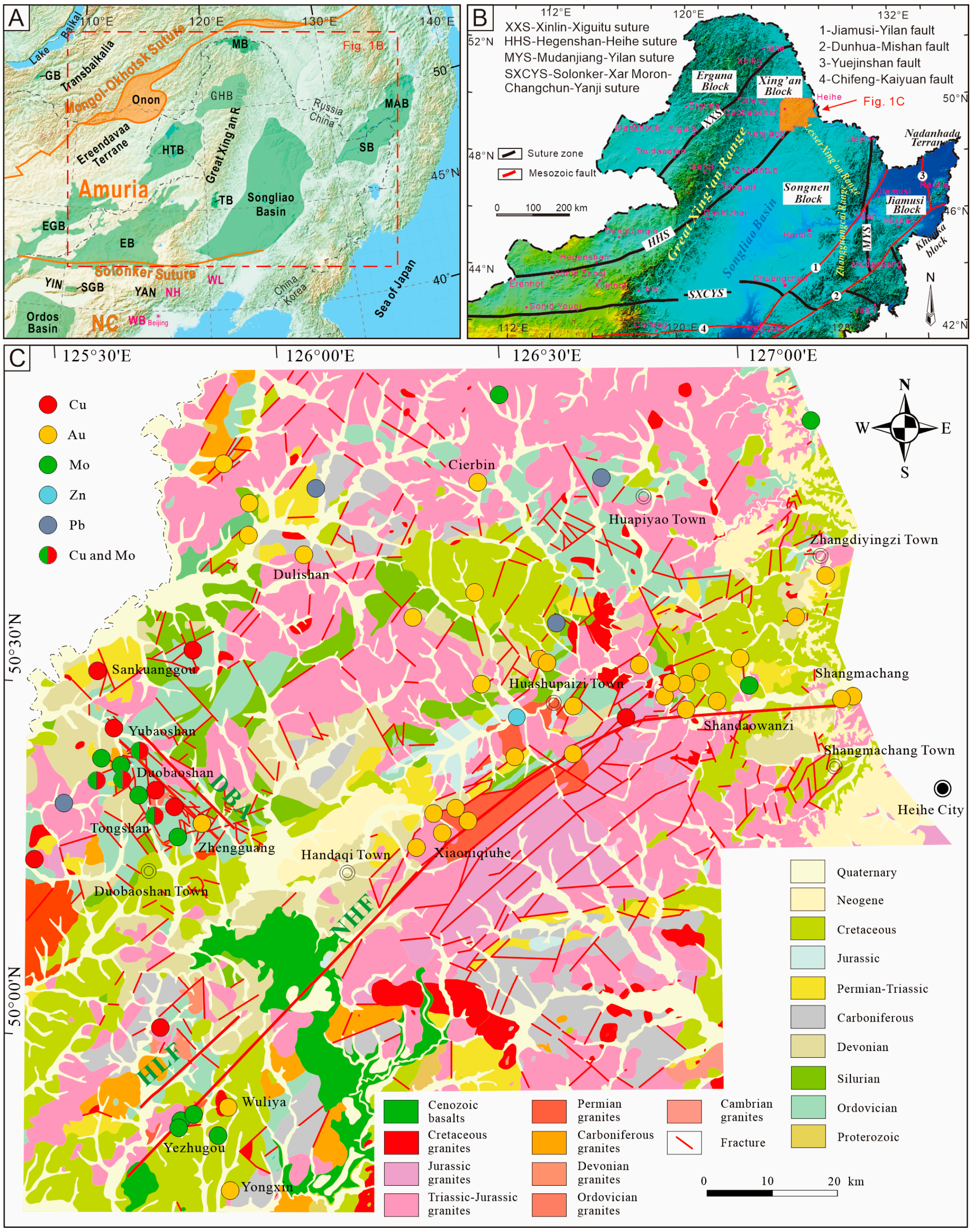

Figure 1. (**A**) Schematic diagram of the structure of the Central Asian orogenic belt, (**B**) tectonic zoning of northeastern China, and (**C**) brief geologic and mineral map of the Nenjiang–Heihe metallogenic belt. DBA—Duobaoshan Anticlinoria; NHF—Nenjiang–Heihe Fault; HLF—Huolongmengou Fault.

The exposed stratigraphy in the study area is dominated by the Proterozoic, Paleozoic, Mesozoic, and Cenozoic deposits (Figure 1C) [38,39]. The Proterozoic Xinkailing Group, Neoproterozoic–Lower Cambrian Galashan Formation, and Beikuanhe Formation mainly consist of various types of schist, gneiss, amphibolite, and acid volcanic rocks. The Paleozoic Ordovician Tongshan Formation is a set of sandy slates. The Duobaoshan Formation consists of altered andesite, dacite, and volcanic sedimentary rocks. The Luohe and Aihui Formations consist of metamorphic siltstone, tuffaceous sandstone, and interbedded slate. The Silurian–Devonian system consists of a set of sandstone, silted sandstone, and tuffaceous sandstone with volcanic rocks in between. The Carboniferous–Permian system is mainly a set of sandstone, tuffaceous sandstone, and pyroclastic rocks. The Mesozoic strata are distributed generally in the northeast direction, among which the Cretaceous Longjiang, Guanghua, Jiufengshan, and Ganhe Formations are a set of intermediate-basic–intermediate-acidic volcanic rocks, pyroclastic rocks, and volcanic sedimentary rocks. The Nenjiang Formation consists of silted sandstone, fine sandstones, and silty mudstones. The Cenozoic is mainly composed of Daxiongshan basalt.

The intrusions are mainly composed of Palaeozoic and Mesozoic igneous rocks. The Cretaceous intrusions include syenogranite, alkali-feldspar granite, monzonitic granite, and granodiorite, demonstrating a complete set of rock assemblages of collisional orogeny, and are linearly distributed in the NE direction in Duobaoshan and Dulishan. Jurassic intrusive rocks mainly consist of diorite, granodiorite, monzonitic granite, and syenogranite. Late Triassic–Early Middle Jurassic intrusions are mainly composed of gabbro, monzonitic granite, granodiorite, and quartz-diorite. Permian intrusive rocks mainly consist of monzonitic granite, syenogranite, monzonitic granit, and alkali-feldspar granite. Carboniferous intrusions include early Carboniferous granitic complex and broken syenogranite. The Early Paleozoic Ordovician intrusions are mainly composed of Middle Ordovician diorite, granodiorite, granodiorite porphyry, and Late Ordovician ultramafic rocks, exposed near Huolongmen and the Duobaoshan copper deposit [40]. Devonian intrusive rocks mainly consist of diorite, whereas Cambrian intrusive rock types mainly include monzonitic granite and granodiorite.

The regional structure is widely developed, and the multiperiod superposition of tectonics leads to the exposure of many ductile shear deformation zones and fold structures in the area. The Nenjiang–Heihe Fault is located between the Xing'an Block and the Songnen Block, spreading in the NE direction along the line of Nenjiang–Nenbei Farm–Beishihe–Heihe, and extending approximately 180 km. It is a regional deep major fault (Figure 1C) [41,42], with Paleozoic and Mesozoic medium-acidic magmatic rocks and Cenozoic basalts on both sides of the fault. The Huolongmengou Fault is located in Huolongmen Township, spreading along the Huolongmengou and striking northeast with an extension length greater than 20 km, forming in the late Early Cretaceous (Figure 1C) [40]. The Duobaoshan Anticlinorium is located along the Duobaoshan, with a northwest fold axis and a curved extension of approximately 20 km. The core strata of the Tongshan Formation and the two flanks of the Duobaoshan Formation have different stratigraphic orientations (Figure 1C) [43,44].

In recent years, with the ongoing mineral exploration in the region [36,44–48], a large number of large- and medium-sized Au-, Cu-, and Mo-based deposits have been discovered, such as porphyry-type copper–molybdenum deposits in Tongshan [49], Duobaoshan [50], and Yezhugou [51]; skarntype ironcopper (molybdenum) deposits in Sankuanggou [52] and Yubaoshan [53]; epithermal gold deposits in Zhengguang [45], Sandaowanzi [54], Yongxin [55]; and other minor Pb-Zn mineralization sites (Figure 1C). The age of mineralization indicates that the porphyry-type Cu-Mo deposits in the study area were mainly formed during the Caledonian, such as Duobaoshan and Tongshan in the Middle Ordovician [56–60]. The silica-type Fe-Cu (Mo) polymetallic deposits, such as Yubaoshan and Sankuanggou were formed in the Early Jurassic [52,53]. The epithermal gold deposits, such as Sandaowanzi, Yongxin, and Xiaoniqiuhe, were formed in the Early Cretaceous [36,46,54,61,62]. The exception is the Zhengguang gold deposit, which formed in the Middle Ordovician [44,45].

3. Methods

3.1. Preprocessing and Linear Construction Extraction

Image preprocessing was divided into four main steps: radiometric calibration, atmospheric correction, image cropping, and image fusion. First, the radiometric correction was performed on the Landsat-8 OLI image data in the study area, using ENVI to convert the raw DN values to outer atmospheric surface reflectances (or radiometric brightness values). Atmospheric correction was then performed using the FLAASH module to reduce the effect of atmospheric scattering. Finally, the images were cropped to the study area and stretched to yield usable images. In this study, the Gram–Schmidt algorithm was used to fuse the multispectral image and panchromatic band image with a resolution of 15 m to improve the spatial and spectral resolution and facilitate constructive interpretation.

To highlight the line texture of remote sensing images we obtained four bands—OLI1, OLI2, OLI3, and OLI4—which were normalized and corrected by image preprocessing and were selected for principal component analysis (PCA). The second principal component was used for comparison to be more favorable for extracting line information. The second principal component was selected for directional filter line enhancement with a Sobel operator convolutional filter window of 3 × 3, which can highlight the fracture structure information in the corresponding direction of remote sensing images and is beneficial for constructive remote sensing interpretation [63].

Automatic extraction of lineaments was performed using PCI Geomatica software digital analysis and visual interpretation. Using the LINE algorithm of PCI Geomatica to set appropriate basic input parameters (Table 1) to optimize the number and quality of extracted lines [64], the algorithm of this module consists of three stages: edge recognition, threshold processing, and curve extraction. In the first stage, an edge image is generated by setting the filter radius (RADI) in the Canny edge detection algorithm [65]. In the second stage, the edge gradient threshold (GTHR) is set to obtain the binary image. In the third stage, the binary edge image is refined by adjusting the curve length threshold (LTHR) to fit line segments to the extracted pixel curves, converting them into vector form; then, polylines are generated by specifying the maximum fitting error using the appropriate straight-line threshold (FTHR) parameter. Finally, the conditions of the maximum angular angle difference threshold (ATHR) and maximum distance link distance threshold (DTHR) between the two vectors specified to be connected are set to perform the polyline connection, and the output is a vector curve. The flow of the specific linear extraction construction method is shown in Figure 2.

Table 1. Adopted parameters for the LINE algorithm.

NO.	Parameters	Code	Values
1	Filter Radius	RADI	80
2	Edge Gradient Threshold	GTHR	10
3	Curve Length Threshold	LTHR	80
4	Line Fitting Error Threshold	FTHR	3
5	Angular Difference Threshold	ATHR	15
6	Linking Distance Threshold	DTHR	10

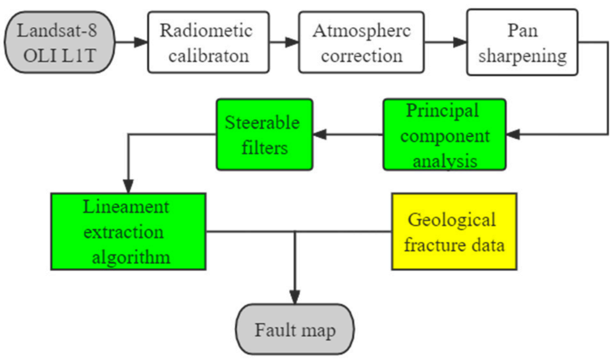

Figure 2. Methodology flowchart of lineaments extraction.

3.2. Box-Counting Fractal Model

The fractal theory has been widely applied and innovated in the field of geology since its creation in the 1970s [66], particularly in the quantitative analysis of fracture structures [18,67,68]. Fracture structures are represented as a series of irregular linear assemblages in a plane that cannot be described by traditional Euclidean geometry in the distribution pattern of faults. The degree of fractal self-similarity for structural fractals is quantitatively described by fractal theory, and the dimensional fractal value of fracture structures is used as a quantitative parameter for the spatial scale and complexity of fractures. Many methods have been used to calculate the fractal dimension value, including the box dimension, capacity dimension, similarity dimension, information dimension, association dimension, Hausdorff dimension, Brigham dimension, and the continuous spectrum of the generalized dimension [69]. The box dimension method has the advantages of simple principles and easy calculation and is the most widely used method to calculate fractal dimension [17,18,70,71].

When all extracted linear constructions in the study area are investigated, a square lattice with side length r equal to $L/2^n$ (where n is an integer) is used to cover the information of lineaments for statistical analysis. The number of grids N(r) covering the linear structures at the corresponding scale is obtained, and if N(r) and r satisfy the power exponent rule, that is, Equation (1), then the object of study is a fractal.

$$N(r) = Cr^{-D} \tag{1}$$

where C and D are constants. We take the logarithm of each side of Equation (1),

$$\log N(r) = -D \log r + \log C \tag{2}$$

According to Equation (2), the log r–log N(r) curve was plotted and fitted using the least-squares method. The fractal value D is the absolute value of this linear relationship equation, and the correlation coefficient R^2 is obtained. The closer the R^2 value is to 1, the better the fit of the fractal plot, and the greater the agreement is with the proportional relationship in Equation (1).

This method was used to calculate the fractal dimension value and draw the fractal dimension contour map. This is done by setting the observation scale r as the side length L, drawing a square with L = 137.6 km, covering all linear constructions in the study area. This is performed by varying the side lengths of the square, that is, r = L/2,L/4,L/8,L/16 . . . , dividing the study area into blocks, and counting the number of grids containing linear constructions at the corresponding scales. The number of grids containing the constructs was calculated as N(r). The log r–log N(r) curves were plotted and fitted using the least-squares method to obtain the fractal dimensional value D and correlation coefficient R^2.

3.3. Fry Analysis

Fry analysis was originally an analytical method used to study the autocorrelation of the spatial distribution of rock strain, which can reveal the autocorrelation of spatial distribution among the target bodies of near-point elements in space. It was gradually extended to examine the relative position and spatial connection between spatial point elements [72]. In recent years, the Fry analysis method has also obtained good results in exploring the spatial distribution patterns of mineral deposits [2,11,15,23–27]. Fry analysis is implemented by constructing an autocorrelation Fry diagram (Figure 3), which involves the translation of point objects (also called Fry diagram), in which each point object is used as a translation origin [27]. The specific steps are as follows:

(1) The original set of points is plotted in the graph, and the location in the center is plotted and numbered.

(2) The original set of points is copied, the second point is placed at the center of the graph, and all other points are maintained at the same distance and orientation.

(3) The position of each point in the replicated point set is marked in a new graph (i.e., "Fry Points").

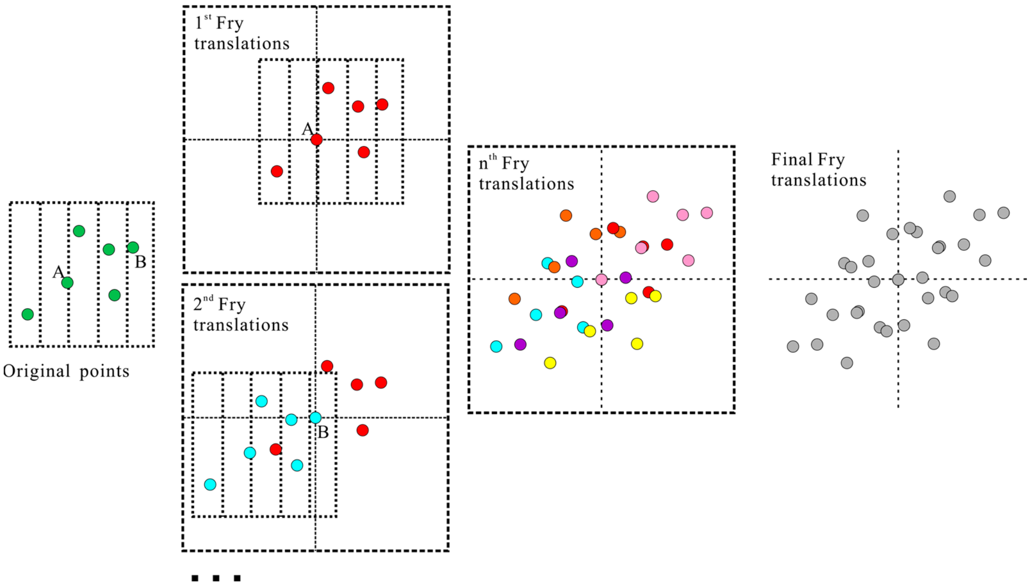

Figure 3. Fry analysis point diagram (modified after carranza [15]).

The third point of the copied point set is placed at the center of the graph, and the positions of the remaining points are recorded while maintaining the distance from the other points. This process is repeated until every point in the original point set is used as the center of the graph.

If the number of known points is n, then a total of ($n^2 - n$) points are obtained on the graph after the vertical projection, which is called a Fry diagram. The Fry diagram increases the overall trend and symmetry of a point object. The results of the Fry analysis can characterize the distance and orientation relationships among the original data points concerning other arbitrary points, enhancing the ability to identify the spatial distribution patterns of the original data points [15]. In particular, Fry analysis can be used to identify the spatial distribution characteristics of the original data points in cases where there is a lack of data points or very complex spatial distribution patterns are implied in the data points.

4. Results and Discussion

4.1. Analysis of Linear Structure Extraction Results

The spread of the water system, micro-geomorphology, lithological boundaries, and other aspects along specific directions in remote sensing images is often reflected by linear features, which mainly manifest as linearly extended ridges, gullies, faulted cliffs, or steep bumps, dark-colored lineaments, light-colored lineaments, and different shades of divisions. In this study, based on geological data, a detailed interpretation of fracture structures in the study area was performed by combining a visual interpretation of structures and automatic extraction of linear structures (Figure 4), and combining mathematical and statistical methods to describe the length, density, frequency, orientation, and other characteristics of linear structures.

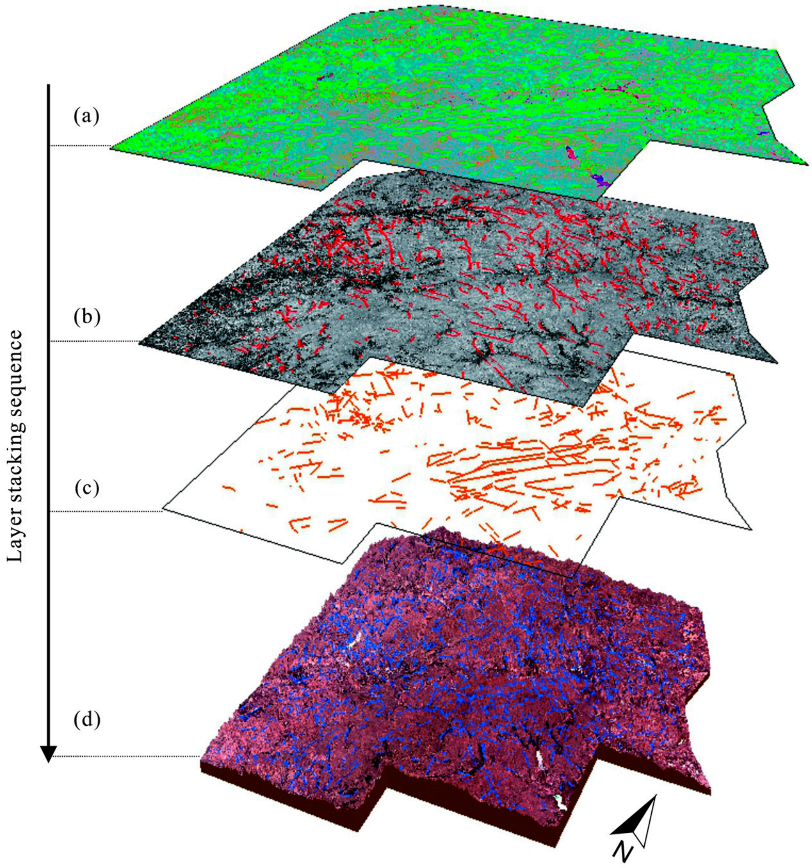

Figure 4. Linear structures superposition synthesis. (**a**) Extracting NE-SW directional filtering linear structure of remote sensing image; (**b**) Extracting NW-SE directional filtering linear structure of remote sensing image; (**c**) 1:250,000 scale geological map linear structure; (**d**) Synthesize all linear structure.

From the remote sensing interpretation, the regional structures of the Nenjiang–Heihe metallogenic belt are segmented in nature. Brittle structures have been significantly developed since the Mesozoic, and the main fracture structure is in the NE direction, followed by the NW direction, and near the S–N direction. The NE direction faults are mainly developed along the river valley with steep dip angles and developed surface cliffs. Many NW direction faults along the line are staggered and displaced. The Nenjiang–Heihe fault is composed of several parallel faults, which are generally distributed along the Nenjiang River basin. The NW direction faults are generally flat and serrated, showing the structural features of tensile (torsional) faults. The landforms are mostly narrow "U" and "V" valleys and saddles. The remote sensing image map mainly shows fault cliffs, which cut the Mesozoic and earlier geological bodies. The main active period of the fractures is in the Mesozoic, mostly cutting NE direction fractures. NE and NW direction's fractures are the main rock-conducting and basin-controlling structures in this area, distributed with Early Cretaceous fracture basins and medium basal volcanic rocks; many Cenozoic basal-ultrabasic volcanic rocks are developed at the intersection of the fractures. The junction of the faults is characterized by many Cenozoic basaltic and ultramafic volcanic rocks, which suggests that the faults are characterized by multi-phase tectonic activity.

Considering the mathematical characteristics, the essence of linear structure density analysis is the frequency of linear structures occurring within the grid, which can be used to study the distribution characteristics of the linear structures in each direction. In this investigation, we used the density analysis tool in ArcGIS software to draw a linear structure density analysis map, which visually represents the sparse and dense distribution of linear structure information in the study area. This remote sensing interpretation obtained 1618 linear structures in the entire region, with an average length of 1813.35 m and a maximum density of 1.12 structures per km^2 (Figure 5a,b). The lineaments' high-density areas (density values between 0.62 and 1.12) roughly show a similar ring shape with low, middle, and high sides. The local high-density areas (density values greater than 0.87) are mainly distributed in the central-eastern and central-western parts, which typically extend in the NE and NW directions. Meanwhile, the northern and southern regions are characterized by more minor secondary faults (Figure 5a). The lineament orientation rose diagram reflects the orientation distribution pattern. The structure orientation in Figure 5c is dominated by the NEE direction, followed by the NWW direction. It is consistent with the orientation of the major deep-large faults in the region, including the Nenjiang–Heihe, Duobaoshan, and Huolongmengou faults. The statistical results are consistent with the image features shown in the above lineaments density map, reflecting the basic distribution pattern of the fracture direction in the study area.

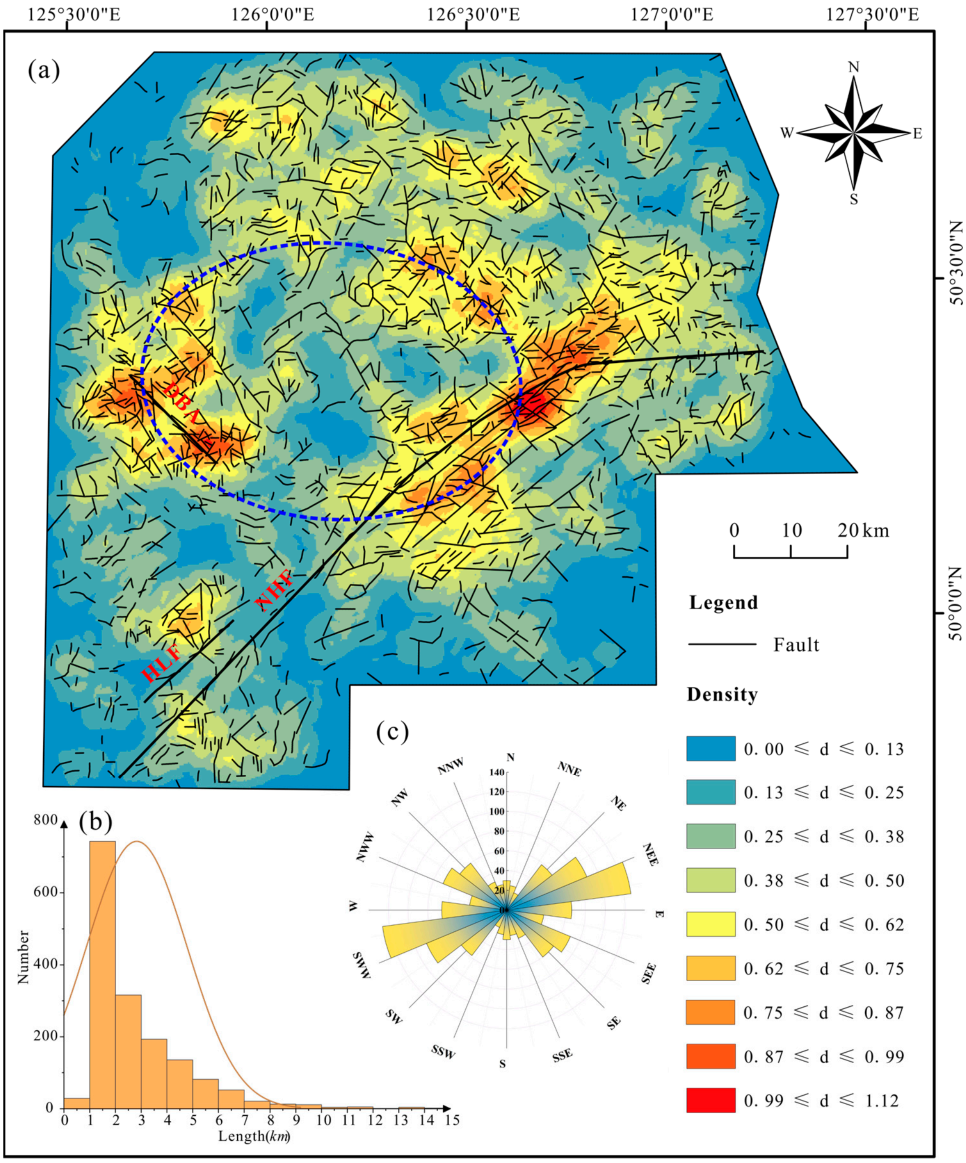

Figure 5. (**a**) Lineament density map, (**b**) Lineament length map, and (**c**) orientation distribution map of linear structure.

4.2. Analysis of Linear Constructs Based on Fractal Dimension

The above map analysis indicates the general correlation between ore deposits concentration and main faults location. However, fractal theory can be used to precisely describe complex structures and quantitatively reveal the regularity of local structures hidden [17–19,70,73–75]. The size of the fractal dimension is a comprehensive indicator of the number, scale, combination, and dynamics, and it is a quantitative parameter of the complexity of the structures [18,20,22,70]. To comprehensively characterize the spatial distribution of linear structures, it is necessary to more realistically reflect the control of linear structures on the transport and accumulation of mineralized hydrothermal fluids. In this study, the fractal box dimension method is used to calculate the dimensional fractal values of linear structures in this region. In the fractal calculation, the study area is divided into lattice scales to match the tectonic scale, so comparing the overall and multi-directional fracture dimension values can explain the complexity of the global metallogenic structure in the study area to a certain extent and realize the coupling relationship analysis with the distribution of the occurrence of ore deposits [18,20,22,70,71,73].

As shown in Figure 6, the fractal values are well linearly correlated with Log N(r). The overall fractal tectonic fractal dimensional value of the study area is 1.622, with a high correlation coefficient (R^2 = 0.996). Therefore, the linear structures in the study area exhibit statistical self-similarity and fractal characteristics. To further investigate the fractal characteristics of the linear structures in different directions, the fractal dimensions of the linear structures in the NE and NW directions were calculated, because the NE and NW directions were the dominant directions of the fracture in the area as mentioned in the previous section. Based on fractal theory and Equation (2), the D_{NE} and D_{NW} values were calculated to be 1.543 and 1.498 (R^2 > 0.9), respectively (Figure 6). The results show that the fractal dimension value in the NE direction is greater than that in the NW direction, indicating that the former direction is more active and developed [17,22,73].

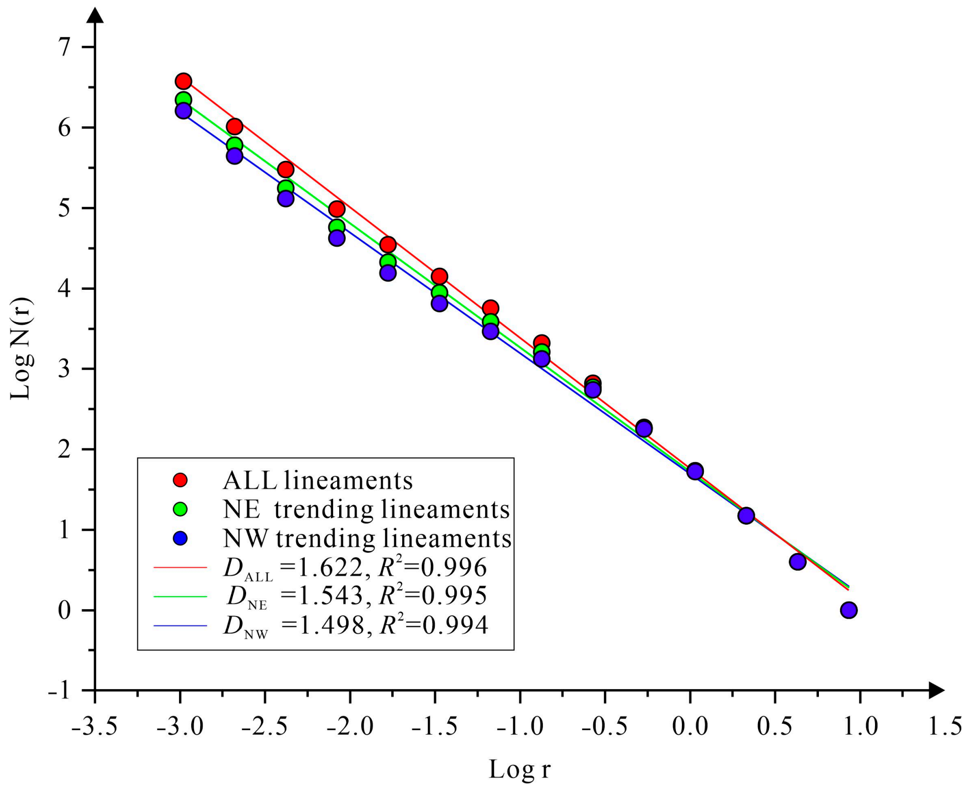

Figure 6. The fractal dimension of lineaments in the study area.

Previous research results show that the size of the fractal dimensions quantitatively describes the complexity and instability of fracture activity, which is conducive to the formation of large and super-large ore deposits, reflecting the spatial and temporal heterogeneity and fractal geometry differences of the fracture system evolution in the study area, thus directly affecting the distribution of ore deposits (points) in the area [3,18,21,22,73,76–78].

Fractal characteristics are a means of quantitatively characterizing the intensity and spatial distribution of fracture activity [58,71,75,79–81].

In comparison with other mineralized areas, the fractal dimensions of the study area are in the middle-to-upper range and are significantly higher than those of the China Continental Fault, indicating that the lineaments of the area are more complex and active (Table 2).

Table 2. Comparison of fractal characteristics with other areas.

NO.	Area	Fractal Dimension	Data Source
1	All lineaments	1.622	This study
2	The NE lineaments	1.543	This study
3	The NW lineaments	1.498	This study
4	Duobaoshan area structure, Heilongjiang	1.754	[82]
5	Northwest Structure of Dayao Mountain in Guangxi	1.689	[22]
6	Central fault zone of Sichuan Basin, China	1.530	[83]
7	Tongling ore concentration area fracture	1.279	[71]
8	East Kunlun Qimantage Hutouya polymetallic ore field fault	1.085	[84]
9	Shanghang–Yunxiao fault zone, China	1.360	[70]
10	Linear structure in the Guangxi area	1.335	[85]
11	Jiuyishan regional fault in southern Hunan	1.116	[20]
12	Chinese mainland fracture	1.237	[86]

To further analyze the spatial distribution characteristics of lineament fractal features, the study area was divided into squares with sides of length 8.6 km. Each 8.6 km^2 unit box was divided into blocks with dimensions of 4.3, 2.15, 1.075, . . . , and 0.00105 km. Fractal dimension contours were plotted using kriging interpolation (Figure 7). As shown in Figure 7, the overall fractal dimension of the study area is high, and the linear structure follows a spatial distribution regularity, showing distribution mainly near deep faults, such as the Duobaoshan anticline and Nenjiang–Heihe fault. These are essential ore-controlling, passable, and host structures. The NE direction lineament fractal high-value areas are concentrated in the vicinity of the Yongxin, Xiaoniqiuhe, and Sandaowanzi gold deposits, whereas the NW direction lineaments' higher fractal dimension values correspond to areas are mainly distributed in Duobaoshan, Zhengguang, and Huashupaizi.

Trend surface analysis is a regression analysis technique that uses the least squares to fit a two-dimensional nonlinear function to analyze the spatial distribution and trend of geological variables. Trend surface analysis of fractal dimension can be used to estimate the spatial distribution of fault structural features, revealing regional patterns of structural change [18,85,87–89]. Using the Geostatistical Wizard module of ArcGIS to obtain the 10th order of lineaments fractal dimension, draw the 10-level trend map (Figure 8) [18,70,85]. As we can see that the four trend lines of tectonic distribution form an evident rhombic grid-like pattern, in which the NE trend line in the southeast is close to the Nenjiang-Heihe fault, the NW trend line in the southwest is identical to the Duobaoshan anticlinorium. The NW trend line in the northeast has no large faults corresponding to it, which may be mainly affected by small faults. By superimposing the known ore deposits on the map, it is found that Zhengguang, Wuliya, Sandaowanzi, Shangmachang gold deposits, and other known ore deposits are mainly distributed in or near the medium-high dimension value area and are in a rhombic grid-type distribution around the trend line, indicating that the linear fractal dimension high-value area has a good coupling relationship with the known ore deposit distribution.

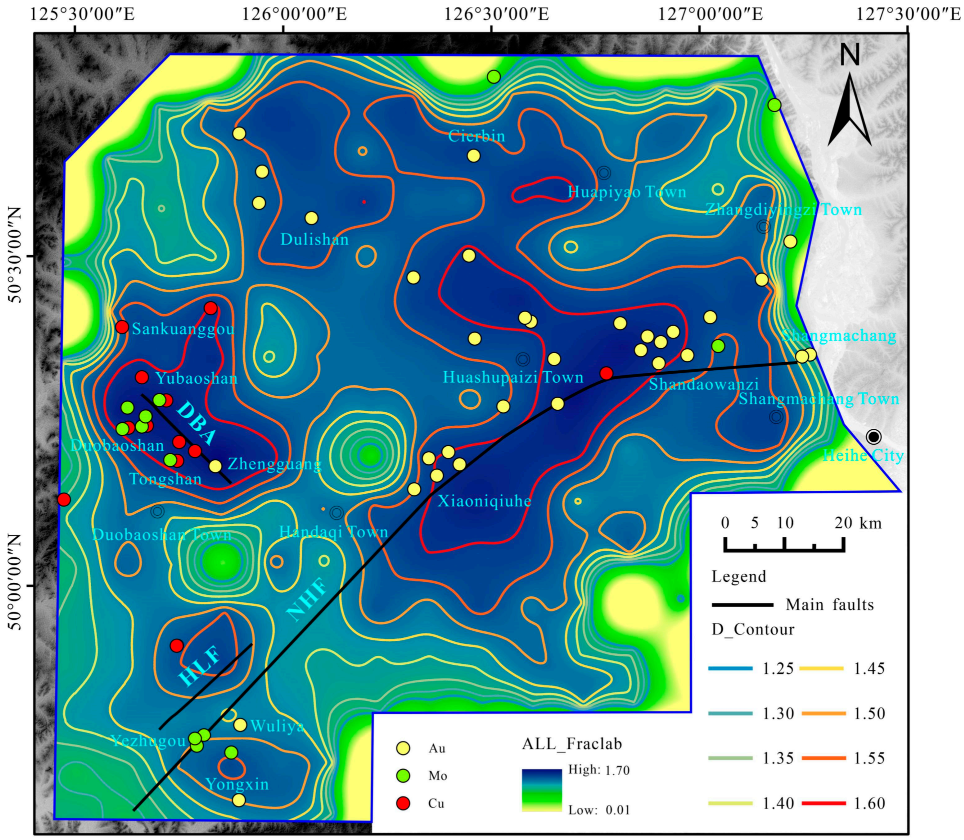

Figure 7. Contour map of the fractal dimension of the lineaments in the study area.

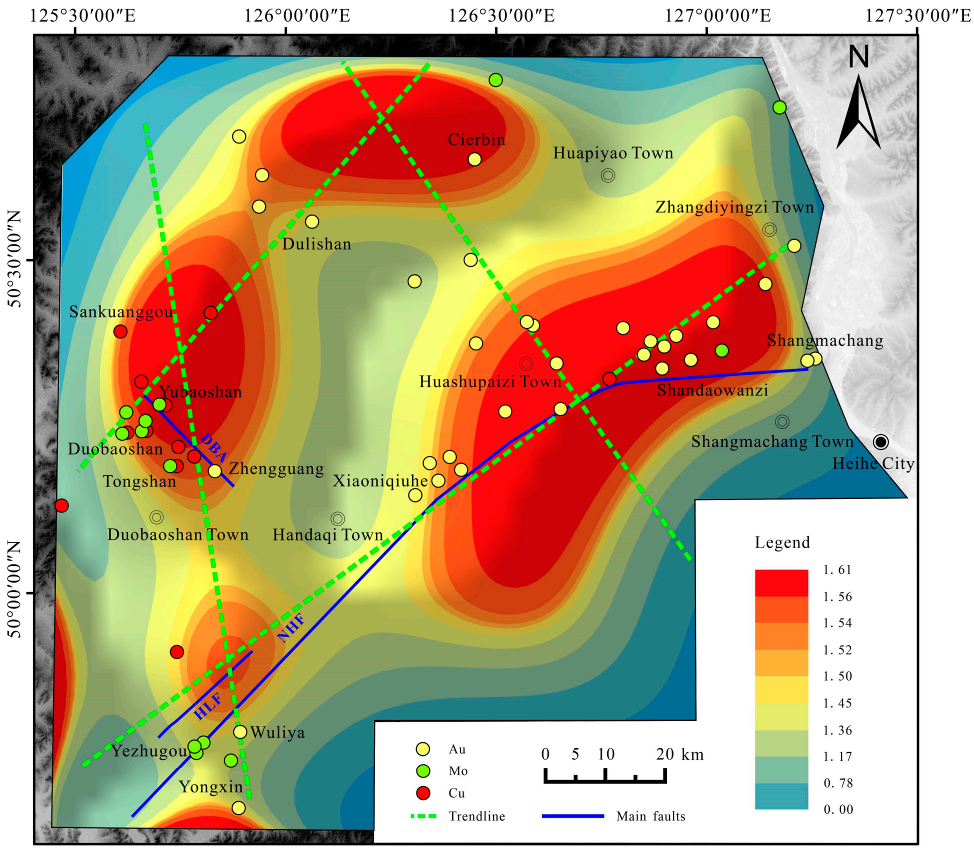

Figure 8. Ten-step tendency map of the fractal dimensions of the lineaments in the study area.

4.3. Analysis of Linear Constructs Based on Fractal Dimension

Fry maps were constructed by selecting 33 gold deposits (points), 12 copper deposits (points), and 13 molybdenum deposits (points) in the study area using ArcGIS software. The spatial distribution maps (Figure 9a) containing locations of known gold, copper, and molybdenum ore deposits were used as the original images, and n instances of ore point movement were used to obtain three Fry images containing a total of ($n^2 - n$) moving points, as shown in Figure 9b. The Fry points were calculated as 10° shifts in the vector direction from the center point to every other point for statistical analysis to produce a rose diagram (Figure 9c). The relationship between the tectonic and mineralization trends in the area is discussed by comparing the results derived from the Fry and rose charts as follows. The metallogenic trend belt is a potential mineralization area, according to the analysis of the spatial distribution of deposits (points), structural fractal dimension, and trend analysis distribution regularities.

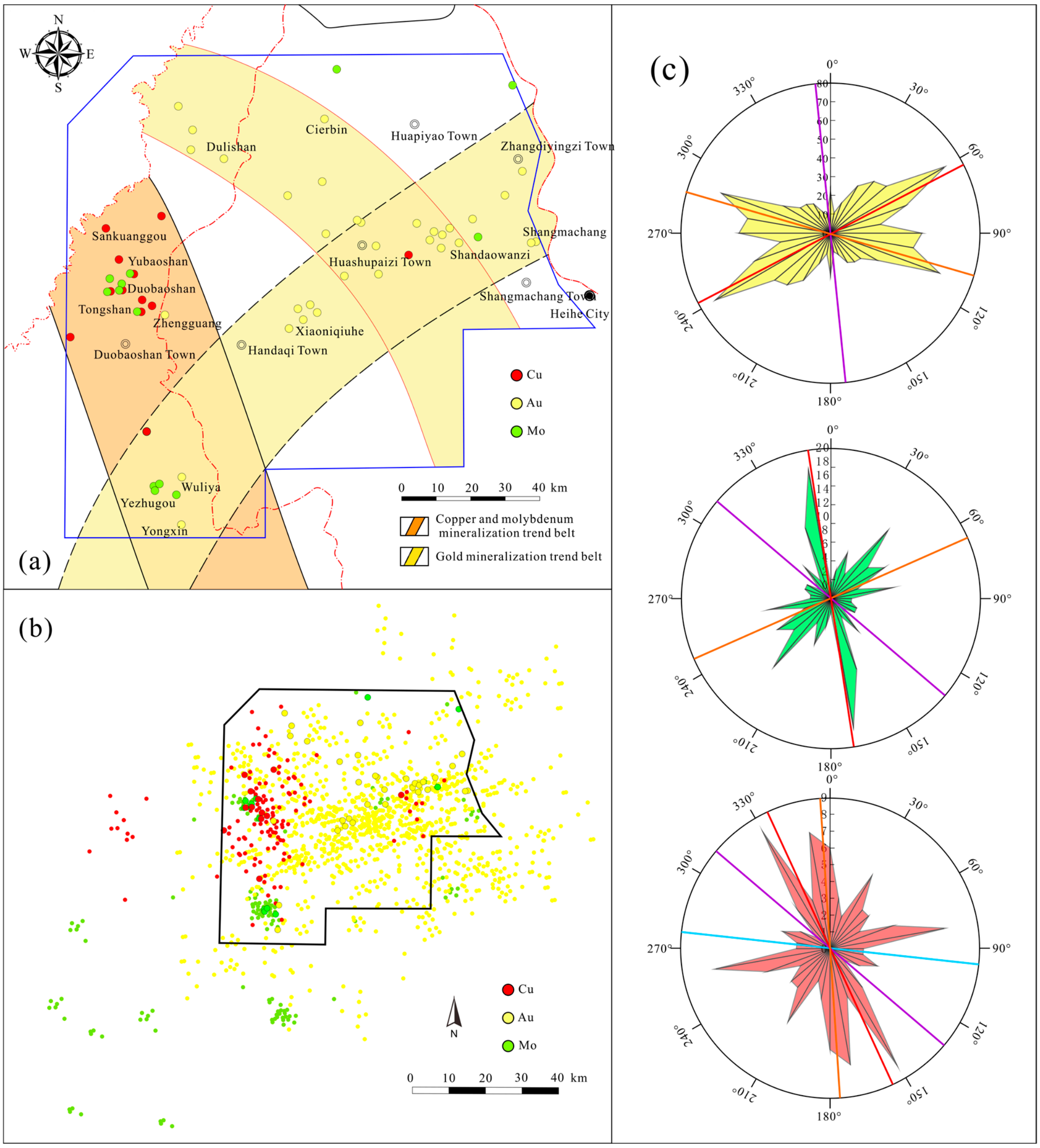

Figure 9. Fry analysis of ore distribution in the study area. (**a**) Main mineral position distribution map; (**b**) Fry analysis map; (**c**) rose chart of metal mineralization trend (yellow represents gold, green represents molybdenum, and red represents copper).

Gold mineralization has two main mineralization trends, the NEE direction and NWW direction (Figure 9a), in which the NEE (60°–70°) direction is the most dominant direction and the NNW (280°–290°) direction is the prevailing secondary direction. The NEE direction spreads from Yongxin to Zhangdiyingzi, mainly distributing the primary deposits of the Wuliya, Yongxin, and Xiaoniqiuhe gold deposits. The NWW direction spreads from Dulishan to Handaqi, mainly distributing the major deposits of the Dulishan and Sandaowanzi gold deposits. The part of the study area where the NEE and NWW directions intersect is a dense area of gold mineralization across the entire region, which is an area of gold mineralization advantage potential across the entire region.

The overall trend of copper mineralization is NW-NNW mineralization, where the NNW (340°–350°) direction is the most extensive dominant mineralization direction of copper mineralization. Compared with copper mineralization, the most considerable prevailing mineralization direction of the molybdenum mineralization trend is the NNW direction (350°–360°). Large deposits, such as Duobaoshan, Zhengguang, and Tongshan, are related to the NNW direction structure. The Cu–Mo mineralization trend belt spreads in a northwest direction along the belt from Sankuanggou to Yongxin, and the intersection with the NEE direction gold mineralization trend belt is a potential area for Au-Cu-Mo mineralization.

5. Conclusions

In this study, the linear structures of the Nenjiang-Heihe metallogenic belt were extracted by combining visual interpretation and automatic extraction. The spatial distribution characteristics of the linear structure and ore deposits were studied and analyzed using the fractal box dimension method and Fry analysis. The results of this study are as follows.

(1) The structure degree of the study area is complex, with NW and NE directions as the main structure directions. Its high-density areas are concentrated in the central-eastern and central-western regions.

(2) The fractal dimensions of NE, NW, and overall linear structures are 1.543, 1.493, and 1.622 respectively. The high-value areas of the fractal dimension are distributed in a rhomboid distribution space, which is strongly coupled with the known deposit distribution.

(3) The distribution of mineralization in the study area is mainly controlled by fractures. The gold mineralization shows two main mineralization trends in the NEE and NWW directions, and the intersection area is characterized by dense gold mineralization. The main trend direction of the Cu–Mo mineralization trend belt is the NNW direction, and the intersection area with a NEE direction gold mineralization trend belt is the Au–Cu–Mo potential mineralization area.

Author Contributions: Conceptualization, J.C. and Z.Z.; methodology, J.C. and Z.Z.; software, J.C. and B.C.; validation, Z.Z., J.C. and X.C.; formal analysis, J.C. and Y.L.; investigation, C.L.; resources, Z.Z. and C.L.; data curation, K.Q.; writing—original draft preparation, J.C., writing—review and editing, J.C. and Z.Z.; visualization, J.C., Y.L. and K.Q.; supervision, C.L.; Y.Y. and Z.Z.; project administration, Z.Z.; and funding acquisition, Z.Z. All authors have read and agreed to the published version of the manuscript.

Funding: This work was supported by the Natural Science Foundation of Liaoning Province (2020-BS-258), the Scientific Research Fund Project of the educational department of Liaoning Province (LJKZ0369), the discipline innovation team of Liaoning Technical University (LNTU20TD-14), and the Heilongjiang Key Programme Project (GA21A204).

Data Availability Statement: Not applicable.

Acknowledgments: The authors would like to thank Earthdata Search for providing Landsat data. Anonymous reviewers to improve the quality of this manuscript are greatly appreciated.

Conflicts of Interest: The authors declare no conflict of interest.

References

1. Adib, A.; Afzal, P.; Ilani, S.M.; Aliyari, F. Determination of the relationship between major fault and zinc mineralization using fractal modeling in the Behabad fault zone, central Iran. *J. Afr. Earth Sci.* **2017**, *134*, 308–319. [CrossRef]
2. Austin, J.; Blenkinsop, T.G. Local to regional scale structural controls on mineralisation and the importance of a major lineament in the eastern Mount Isa Inlier, Australia: Review and analysis with autocorrelation and weights of evidence. *Ore Geol. Rev.* **2009**, *35*, 298–316. [CrossRef]
3. Bierlein, F.P.; Murphy, F.C.; Weinberg, R.F.; Lees, T. Distribution of orogenic gold deposits in relation to fault zones and gravity gradients: Targeting tools applied to the Eastern Goldfields, Yilgarn Craton, Western Australia. *Miner. Depos.* **2006**, *41*, 107–126. [CrossRef]
4. Carranza, E.J.M.; Hale, M. Spatial association of mineral occurrences and curvilinear geological features. *Math. Geol.* **2002**, *34*, 203–221. [CrossRef]
5. Chernicoff, C.J.; Richards, J.P.; Zappettini, E.O. Crustal lineament control on magmatism and mineralization in northwestern Argentina: Geological, geophysical, and remote sensing evidence. *Ore Geol. Rev.* **2002**, *21*, 127–155. [CrossRef]
6. Groves, D.I.; Bierlein, F.P. Geodynamic settings of mineral deposit systems. *J. Geol. Soc.* **2007**, *164*, 19–30. [CrossRef]
7. Mirzaie, A.; Bafti, S.S.; Derakhshani, R. Fault control on Cu mineralization in the Kerman porphyry copper belt, SE Iran: A fractal analysis. *Ore Geol. Rev.* **2015**, *71*, 237–247. [CrossRef]
8. Safari, H.O.; Bagas, L.; Bafti, B.S. Structural controls on the localization of Cu deposits in the Kerman Cu metallogenic province of Iran using geoinformatic techniques. *Ore Geol. Rev.* **2015**, *67*, 43–56. [CrossRef]
9. Afzal, P.; Ahari, H.D.; Omran, N.R.; Aliyari, F. Delineation of gold mineralized zones using concentration–volume fractal model in Qolqoleh gold deposit, NW Iran. *Ore Geol. Rev.* **2013**, *55*, 125–133. [CrossRef]
10. Carranza, E.J.M.; Sadeghi, M. Post-VMS mineralization deformations (1880–1820 Ma) of the Skellefte district (Sweden): Insights from the spatial pattern of VMS occurrences. *Front. Earth Sci.* **2014**, *8*, 319–324. [CrossRef]
11. Carranza, E.J.M.; Owusu, E.A.; Hale, M. Mapping of prospectivity and estimation of number of undiscovered prospects for lode gold, southwestern Ashanti Belt, Ghana. *Miner. Depos.* **2009**, *44*, 915–938. [CrossRef]
12. Zhao, Z.; Qiao, K.; Liu, Y.; Chen, J.; Li, C. Geochemical Data Mining by Integrated Multivariate Component Data Analysis: The Heilongjiang Duobaoshan Area (China) Case Study. *Minerals* **2022**, *12*, 1035. [CrossRef]
13. Lin, N.; Chen, Y.; Liu, H.; Liu, H. A comparative study of machine learning models with hyperparameter optimization algorithm for mapping mineral prospectivity. *Minerals* **2021**, *11*, 159. [CrossRef]
14. Du, X.; Zhou, K.; Cui, Y.; Wang, J.; Zhou, S. Mapping Mineral Prospectivity Using a Hybrid Genetic Algorithm–Support Vector Machine (GA–SVM) Model. *ISPRS Int. J. Geo-Inf.* **2021**, *10*, 766. [CrossRef]
15. Carranza, E.J.M. Controls on mineral deposit occurrence inferred from analysis of their spatial pattern and spatial association with geological features—ScienceDirect. *Ore Geol. Rev.* **2009**, *35*, 383–400. [CrossRef]
16. Maanijou, M.; Daneshvar, N.; Alipoor, R.; Azizi, H. Spatial analysis on gold mineralization in Southwest Saqqez using point pattern, fry and fractal analyses. *Geotectonics* **2020**, *54*, 589–604. [CrossRef]
17. Liu, Z.; Han, L.; Du, C.; Cao, H.; Wang, H. Fractal and Multifractal Characteristics of Lineaments in the Qianhe Graben and Its Tectonic Significance Using Remote Sensing Images. *Remote Sens.* **2021**, *13*, 587. [CrossRef]
18. Ni, C.; Zhang, S.; Chen, Z.; Yan, Y.; Li, Y. Mapping the spatial distribution and characteristics of lineaments using fractal and multifractal models: A case study from northeastern Yunnan Province, China. *Sci. Rep.* **2017**, *7*, 1–11. [CrossRef]
19. Tan, K.X.; Xie, Y.S. Multifractal mechanism of faults controlling hydrothermal deposits in altay, Xinjiang, China. *Geotecton. Et Metallog.* **2010**, *34*, 32–39.
20. Lei, T.C.; Cui, F.; Yu, F.M.; Xu, H.G. Study on fractal feature of fault structure and its geological implications based on remote sensing: A case study of Jiuyi Mountain area, Southern Hunan. *Geol. Rev.* **2012**, *58*, 594–600.
21. Ma, A.; Mm, A.; Pa, B.; Abyc, D.; Ejc, E. Fractal modeling and fry analysis of the relationship between structures and Cu mineralization in Saveh region, Central Iran. *Ore Geol. Rev.* **2019**, *107*, 172–185.
22. Jiang, C.; Li, S.H.; Fu, S.; Xie, Z.L.; Liao, H.W. Tectonic fractal and mentallogenic prediction in Northwest Dayao Mountain, Guangxi. *Acta Geosci. Sin.* **2021**, *42*, 514–526.
23. Blenkinsop, T.G.; Kadzviti, S. Fluid flow in shear zones: Insights from the geometry and evolution of ore bodies at Renco gold mine, Zimbabwe. *Geofluids* **2006**, *6*, 334–345. [CrossRef]
24. Kreuzer, O.; Blenkinsop, T.G.; Morrison, R.; Peters, S. Ore controls in the Charters Towers goldfield, NE Australia: Constraints from geological, geophysical and numerical analyses. *Ore Geol. Rev.* **2007**, *32*, 37–80. [CrossRef]
25. Parsa, M.; Maghsoudi, A. Controls on Mississippi Valley-Type Zn-Pb mineralization in Behabad district, Central Iran: Constraints from spatial and numerical analyses. *J. Afr. Earth Sci.* **2018**, *140*, 189–198. [CrossRef]
26. Stubley, M. Spatial distribution of kimberlite in the Slave craton, Canada: A geometrical approach. *Lithos* **2004**, *77*, 683–693. [CrossRef]
27. Vearncombe, J.; Vearncombe, S. The spatial distribution of mineralization; applications of Fry analysis. *Econ. Geol.* **1999**, *94*, 475–486. [CrossRef]
28. Behyari, M.; Rahimsouri, Y.; Hoseinzadeh, E.; Kurd, N. Evaluating of lithological and structural controls on the barite mineralization by using the remote sensing, Fry and fractal methods, Northwest Iran. *Arab. J. Geosci.* **2019**, *12*, 1–11. [CrossRef]

29. Lisitsin, V. Spatial data analysis of mineral deposit point patterns: Applications to exploration targeting. *Ore Geol. Rev.* **2015**, *71*, 861–881. [CrossRef]
30. Bie, L.D.; Chen, J.P.; Liu, J.P.; Yan, Q. Coal mine distribution characteristics in Chengde region and their fractal research controlled by faults. *J. Geol.* **2011**, *35*, 38–44.
31. Jahn, B.M. The Central Asian Orogenic Belt and growth of the continental crust in the Phanerozoic. *Geol. Soc. Lond. Spec. Publ.* **2004**, *226*, 73–100. [CrossRef]
32. Jahn, B.M.; Wu, F.; Chen, B. Massive granitoid generation in Central Asia: Nd isotope evidence and implication for continental growth in the Phanerozoic. *Epis. J. Int. Geosci.* **2000**, *23*, 82–92. [CrossRef]
33. Kovalenko, V.I.; Yarmolyuk, V.V.; Kovach, V.P.; Kotov, A.B.; Kozakov, I.K.; Salnikova, E.B.; Larin, A.M. Isotope provinces, mechanisms of generation and sources of the continental crust in the Central Asian mobile belt: Geological and isotopic evidence. *J. Asian Earth Sci.* **2004**, *23*, 605–627. [CrossRef]
34. Windley, B.F.; Alexeiev, D.; Xiao, W.; Kroner, A.; Badarch, G. Tectonic models for accretion of the Central Asian Orogenic Belt. *J. Geol. Soc.* **2007**, *164*, 31–47. [CrossRef]
35. Wu, F.Y.; Jahn, B.M.; Wilde, S.A.; Lo, C.H.; Sun, D.Y. Highly fractionated I-type granites in NE China (II): Isotopic geochemistry and implications for crustal growth in the Phanerozoic. *Lithos* **2003**, *67*, 191–204. [CrossRef]
36. Zhao, Z.H.; Sun, J.G.; Li, G.H.; Xu, W.X.; Lü, C.L.; Guo, Y.; Liu, J.; Zhang, X. Zircon U–Pb geochronology and Sr–Nd–Pb–Hf isotopic constraints on the timing and origin of the Early Cretaceous igneous rocks in the Yongxin gold deposit in the Lesser Xing'an Range, NE China. *Geol. J.* **2020**, *55*, 2684–2703. [CrossRef]
37. Zheng, Y.F.; Xiao, W.J.; Zhao, G. Introduction to tectonics of China. *Gondwana Res. Int. Geosci. J.* **2013**, *23*, 1189–1206. [CrossRef]
38. Li, C.L.; Li, S.R.; Yuan, M.W.; Du, B.Y.; Li, W.L.; Liu, D.Y.; Liu, H. Genesis of the Keluo Au deposit in the Nenjiang-Heihe tectonic melangebelt, Heilongjiang Province: Evidence from chemical composition and pyrite He-Ar, S, Pb isotopes. *Earth Sci. Front.* **2020**, *27*, 99–115.
39. Yin, G.L.; Lyu, C.L.; Cui, Y.J.; Shi, G.M.; Yu, Y.J.; Yang, F.S.; Jiang, H.J. Tectono-geochemical characteristics and geological insignificance in arc basin system of Da Hinggan Mountains. *Miner. Resour. Geol.* **2018**, *32*, 553–561.
40. Li, C.L.; Xu, W.X.; Li, S.R.; Song, Z.C.; Wang, Z.; Qu, H.; Xu, Z.G. Zircon U-Pb ages, geochemical characteristics and tectonicimplications of the early permian granites in Huolongmenarea, northeast Da Hinggan Mountains. *Mineral. Petrol.* **2017**, *37*, 46–54.
41. Han, G.; Liu, Y.; Neubauer, F.; Jin, W.; Genser, J.; Ren, S.; Li, W.; Wen, Q.; Zhao, Y.; Liang, C. LA-ICP-MS U–Pb dating and Hf isotopic compositions of detrital zircons from the Permian sandstones in Da Xing'an Mountains, NE China: New evidence for the eastern extension of the Erenhot–Hegenshan suture zone. *J. Asian Earth Sci.* **2012**, *49*, 249–271. [CrossRef]
42. Fu, J.; Wang, Y.; Na, F.C.; Yang, F.; Zhang, G.Y.; Liu, Y.C.; Kang, Z. Geology of the Hadayang tectonic mélange in Inner Mongolia: Discovery significance. *Geol. Resour.* **2015**, *24*, 408–413.
43. Li, Y.; Fu, J.J.; Zhao, Y.Y.; Zeng, H. Chronological characteristics and metallogenic significance of Zhengguang gold deposit, Heilongjiang Province, China. *Acta Geol. Sin.* **2016**, *90*, 151–162.
44. Song, G.X.; Qin, K.Z.; Wang, L.; Guo, J.H.; Li, Z.Z.; Tong, K.Y.; Zou, X.Y.; Li, G.M. Type, zircon U-Pb age and Paleo-volcano edifice of Zhengguang gold depositin Duobaoshan orefield in Heilongjiang Province, NE-China. *Acta Petrol. Sin.* **2015**, *31*, 2402–2416.
45. Gao, R.; Xue, C.; Lü, X.; Zhao, X.; Yang, Y.; Li, C. Genesis of the Zhengguang gold deposit in the Duobaoshan ore field, Heilongjiang Province, NE China: Constraints from geology, geochronology and S-Pb isotopic compositions. *Ore Geol. Rev.* **2017**, *84*, 202–217. [CrossRef]
46. Zhao, Z.H.; Sun, J.G.; Li, G.H.; Xu, W.X.; Lü, C.L.; Wu, S.; Guo, Y.; Liu, J.; Ren, L. Early Cretaceous gold mineralization in the Lesser Xing'an Range of NE China: The Yongxin example. *Int. Geol. Rev.* **2019**, *61*, 1522–1549. [CrossRef]
47. Li, C.L. *Gold Metallogeny and Prospecting in the Nenjiang-Heihe Tectonic Melange Zone, Heilongjiang Province*; China University of Geosciences: Beijing, China, 2018.
48. Xiang, A.P.; Yang, X.C.; Li, G.T.; She, H.Q.; Guan, J.D.; Li, J.W.; Guo, Z.J. Diagenetic and metallogenic ages of Duobaoshan porphyry Cu-Mo depositin Heilongjiang Province. *Miner. Depos.* **2012**, *31*, 1237–1248.
49. Wang, L.; Qin, K.Z.; Pang, X.Y.; Song, G.X.; Jin, L.Y.; Li, G.M.; Zhao, C. Geological characteristics and alteration zonation of Tongshan porphyry copper deposit within Duobaoshan orefield, Heilongjiang: Implications for hydrothermal-mineralization center and further exploration. *Miner. Depos.* **2017**, *36*, 1143–1168.
50. Zeng, Q.D.; Liu, J.M.; Chu, S.X.; Wang, Y.B.; Sun, Y.; Duan, X.X.; Zhou, L.L.; Qu, W.J. Re–Os and U–Pb geochronology of the Duobaoshan porphyry Cu–Mo–(Au) deposit, northeast China, and its geological significance. *J. Asian Earth Sci.* **2014**, *79*, 895–909. [CrossRef]
51. Zhao, Z.H.; Zheng, W.Z.; Qu, H.; Guo, Y.; Li, C.L.; Wang, Z.; Zhang, J.F. Cu-Au mineralization and metallogenic regularity of Duobaoshan area, Heilongjiang Province. *Miner. Depos.* **2012**, *31*, 601–614.
52. Deng, K.; Chen, Y.J.; Zhang, C.; Xu, W.Q.; Zhu, X.F. Mineralogical characteristics and ore-forming physicochemical conditions of the Sankuanggou skarn Fe-Cu deposit, Heilongjiang Province. *Earth Sci. Front.* **2018**, *25*, 167–182.
53. Hao, J.Y. *Mineralization and Metallogenic Regularity of DuobaoshanOre Concentration Area in Heilongjiang Province, Northeast China*; Jilin University: Changchun, China, 2015.
54. Zhai, D.G.; Wang, J.P.; Liu, J.J.; Ripley, E.M. Geochronological and He-Ar-S isotopic constraints on the origin of the Sandaowanzi gold-telluride deposit, northeastern China. *Lithos Int. J. Mineral. Petrol. Geochem.* **2015**, *212*, 338–352. [CrossRef]

55. Zhao, Z.H.; Chen, J.; Qiao, K.; Cui, X.M.; Sun, J.G.; Li, C.L.; Yang, Y. Ore-fluid sources and genesis of Yongxin gold deposit in northwestern XiaoHinggan Mountains: Constraint from fluid inclusions and H-O-S-Pb isotopes. *Miner. Depos.* **2021**, *40*, 221–240.
56. Ge, W.; Wu, F.; Zhou, C.; Zhang, J. Porphyry Cu-Mo deposits in the eastern Xing'an-Mongolian Orogenic Belt: Mineralization ages and their geodynamic implications. *Chin. Sci. Bull.* **2007**, *52*, 3416–3427. [CrossRef]
57. Hao, Y.J.; Ren, Y.S.; Duan, M.X.; Tong, K.Y.; Chao, L. Metallogenic events and tectonic setting of the Duobaoshan ore field in Heilongjiang Province, NE China. *J. Asian Earth Ences* **2015**, *97*, 442–458. [CrossRef]
58. Liu, J.; Wu, G.; Li, Y.; Zhu, M.; Zhong, W. Re–Os sulfide (chalcopyrite, pyrite and molybdenite) systematics and fluid inclusion study of the Duobaoshan porphyry Cu (Mo) deposit, Heilongjiang Province, China. *J. Asian Earth Sci.* **2012**, *49*, 300–312. [CrossRef]
59. Cui, G.; Wang, J.Y.; Zhang, J.X.; Cui, G. U-Pb SHRIMP dating of zircons from Duobaoshan granodiorite in Heilongjiang and its geological significance. *Glob. Geol.* **2008**, *27*, 387–394.
60. Zhao, Y.M. metasomatic zoning in some major Pb-Zn polymetallic skarn deposits of China. *Miner. Depos.* **1997**, *16*, 25–34.
61. Hao, B.; Deng, J.; Bagas, L.; Ge, L.; Nie, F.; Turner, S.; Min, Q. The Gaosongshan epithermal gold deposit in the Lesser Hinggan Range of the Heilongjiang Province, NE China: Implications for Early Cretaceous mineralization. *Ore Geol. Rev.* **2016**, *73*, 179–197. [CrossRef]
62. Zhao, Z.H.; Sun, J.G.; Li, G.H.; Xu, W.X.; Lü, C.L.; Wu, S.; Guo, Y.; Ren, L.; Hu, Z.X. Age of the Yongxin Au deposit in the Lesser Xing'an Range: Implications for an Early Cretaceous geodynamic setting for gold mineralization in NE China. *Geol. J.* **2019**, *54*, 2525–2544. [CrossRef]
63. Hermi, S.O.; Elsheikh, R.F.A.; Aziz, M.; Bouaziz, S. Structural interpretation of lineaments uses satellite images processing: A case study in North-Eastern Tunisia. *J. Geogr. Inf. Syst.* **2017**, *9*, 440. [CrossRef]
64. Thannoun, R.G. Automatic Extraction and Geospatial Analysis of Lineaments and their Tectonic Significance in some areas of Northern Iraq using Remote Sensing Techniques and GIS. *Int. J. Enhanc. Res. Sci. Technol. Eng. Bull.* **2013**, *2*, 1–11.
65. Akinwumiju, A.; Olorunfemi, M.; Afolabi, O. Automated lineament mapping from remotely sensed data: Case study Osun drainage basin, southwestern Nigeria. *Ife J. Sci.* **2016**, *18*, 177–201.
66. Mandelbrot, B. How long is the coast of Britain? Statistical self-similarity and fractional dimension. *Science* **1967**, *156*, 636–638. [CrossRef] [PubMed]
67. Li, F.; Liu, G.S.; Zhou, Q.W.; Zhan, G.B. Application of fractal theory in the study of the relationship between fracture and minera. *J. Hefei Univ. Technol. (Nat. Sci.)* **2016**, *39*, 701–706.
68. Bai, H.; Cao, Y.; Zhang, H.; Wang, W.; Jiang, C.; Yang, Y. Applying Data-Driven-Based Logistic Function and Prediction-Area Plot to Map Mineral Prospectivity in the Qinling Orogenic Belt, Central China. *Minerals* **2022**, *12*, 1287. [CrossRef]
69. Shen, W. *Fractal Chaos and Mineral Prediction*; Geological Publishing House: Beijing, China, 2002; pp. 6–48. ISBN 978-7-1160-3559-1.
70. Lyu, C.; Cheng, Q.; Zuo, R.; Wang, X. Mapping spatial distribution characteristics of lineaments extracted from remote sensing image using fractal and multifractal models. *J. Earth Sci.* **2017**, *28*, 507–515. [CrossRef]
71. Sun, T.; Li, H.; Wu, K.X.; Chen, L.K.; Liu, W.M.; Hu, Z.J. Fractal and multifractal characteristics of regional fractures in Tongling metallogenic Area. *Nonferrous Met. Eng.* **2018**, *8*, 111–115.
72. Fry, N. Random point distributions and strain measurement in rocks. *Tectonophysics* **1979**, *60*, 89–105. [CrossRef]
73. Nan, W.; Liu, Y. Fractal Characteristics of Fault Structures and Their Use for Mapping Ore–prospecting Potential in the Qitianling Area, Southern Hunan Province, China. *Acta Geol. Sin. Engl. Ed.* **2015**, *89*, 121–132. [CrossRef]
74. Jin, Z.D.; Lu, X.W.; Zhang, C.L. A study of fractal dimension of the fracture system in the Dexing porphyry copper orefield, Jiangxi. *Geol. Rev.* **1998**, *44*, 57–62.
75. Xie, Y.S.; Tan, K.X. Fractal research on fracture structures and application in geology. *Earth Environ.* **2002**, *1*, 71–77.
76. Zhao, S.J.; Qian, J.P.; Chen, H.Y. Application of fractal statistics of linear structure and alteration information extraction of remote sensing on the Au, Pb, Zn, Sn polymetallic minerogenetic prognosis in Eastern Guangxi. *Geotecton. Et Metallog.* **2011**, *35*, 364–371.
77. Ahmadirouhani, R.; Karimpour, M.H.; Rahimi, B.; Malekzadeh-Shafaroudi, A.; Pour, A.B.; Pradhan, B. Integration of Spot-5 and Aster Satellite Data for Structural Tracing and Hydrothermal Alteration Mineral Mapping: Implications for Cu–Au Prospecting. *Int. J. Image Data Fusion* **2018**, *9*, 237–262. [CrossRef]
78. Shiran, M.; Asadi, M.A.Z.; Mozzi, P.; Adab, H.; Amirahmadi, A. Detection of Surface Anomalies through Fractal Analysis and Their Relation to Morphotectonics (High Zagros Belt, Iran). *Geosci. J.* **2020**, *24*, 597–613. [CrossRef]
79. Tan, K.X.; Hao, X.C.; Dai, T.G. Fractal Features Of Fractures In Chinaand Their Implication Fur Geotectonics. *Geotecton. Et Metallog.* **1998**, *1*, 17–20.
80. Pan, X.D.; Kang, L. Study on fractal characteristics of Hunjiang fault zone and drainage systems and activity of tectonic. *J. Disaster Prev. Reduct.* **2002**, *4*, 7–15.
81. Kong, F.C.; Ding, G.Y. The implications the fractal dimension values of lineaments. *Earthquake* **1991**, *5*, 33–37.
82. Zhao, Z.H.; Chen, J.; Qiao, K.; Cui, X.M.; Liang, S.S.; Li, C.L. Remote Sensing Alteration lnformation and Structure Analysis Based onFractal Theory: A Case Study of Duobaoshan Area of Heilongjiang Province. *Geoscience* **2022**, *19*, 1–16.
83. Fan, C.; Tao, J.; Zhou, K.; Hu, F.; Huang, W. Fractal characteristics of reservoir structural fracture: A case study of Xujiahe Formation in central Yuanba area, Sichuan Basin. *Earth Sci. Res. J.* **2018**, *22*, 113–118. [CrossRef]

84. Zerrouk, S.; Bendaoud, A.; Hamoudi, M.; Liégeois, J.P.; Boubekri, H.E.; Khaznadji, R.B. Mapping and discriminating the Pan-African granitoids in the Hoggar (southern Algeria) using Landsat 7 ETM+ data and airborne geophysics. *J. Afr. Earth Sci.* **2017**, *127*, 146–158. [CrossRef]
85. Li, L.F. *Fractal Feature and Fractal Dimension Analysis of Lineament in Guangxi Region*; Guilin University of Technology: Guilin, China, 2017.
86. Zhu, X.H.; Wang, J. On relationship between the fractal and scales—A case study of China's continental mountain ridges. *J. Geo-Inf. Sci.* **2003**, *16*, 67–72.
87. Li, S.M.; Yao, S.Z.; Han, Y.C. Using tendency analysis method to deal with geochemical databased on the surfer software. *Geol. Explor.* **2007**, *43*, 72–75.
88. Li, Z.R.; Zhang, K.; Li, X.M.; Li, D.L.; Ma, S.B. Analysis of linear structural characteristics of remote sensing and prediction of ore finding. *Remote Sens. Inf.* **2016**, *31*, 115–121.
89. Hao, M.; Wu, H.; Jia, Z.Q.; Huang, D.N.; Liu, Y.; Guan, Z. Discussion on genetic correlation between Huashan granite body and Guposhan granite body based on comparative analysis of fault structure features in remote sensing image. *Remote Sens. Land Resour.* **2014**, *26*, 162–169.